Experimental Mechanics (2019) 59:691–702
https://doi.org/10.1007/s11340-019-00508-0

Investigation of the Relationship Between Microstructural Features and Strain Localization in Polycrystalline 316 L

L. Bodelot[1]

Received: 15 November 2018 / Accepted: 2 April 2019 / Published online: 24 April 2019

Abstract

In this paper, strains are monitored in-situ at the surface of a polycrystalline 316 L sample loaded quasi-statically in uniaxial tension. Initial orientation data collected over thousands of grains is compared with the strain data evolution in order to investigate, with statistical significance, the relationship between the microstructural features and the strain localization patterns emerging at the grain scale. It is shown quantitatively that high values of strain appear early and primarily around grain boundaries, before growing into a network spanning several grains and grain boundaries. Strains are also heterogeneous within a grain, with the heterogeneity tending to be more pronounced in larger grains. Statistical analyses demonstrate that the usual microstructural descriptors—such as Taylor factors, average intragranular misorientation angles or intergranular misorientation angles—do not display any correlation with the localization network. Furthermore, higher Schmid factors, albeit exhibiting some weak correlation with higher strains, fail to systematically identify the grains that experience the largest strains. It is thus proposed to analyze three-dimensional descriptors of orientation expressed in the Rodrigues space and they are shown to help readily identify orientations that exhibit high strains early in the loading. Additionally, the study of the full three-dimensional misorientation information, expressed in the reduced Rodrigues space, clearly highlights the fact that some misorientations oppose localization at certain boundaries in the microstructure at hand. Hence, considering the full three-dimensional orientation (and misorientation) data instead of just scalar descriptors is demonstrated to be of great interest when investigating the relationship between microstructural features and strain localization.

Keywords EBSD · Mechanical characterization · Digital image correlation · Austenitic stainless steel · Plasticity · Orientation relationship

Introduction

It is well acknowledged that the assumption of homogeneity in deformation for polycrystals only holds at a rather macroscopic scale. Indeed, even under uniform macroscopic loading, the mechanical behavior of polycrystals is highly heterogeneous at the local scale due to individual grain orientations. Heterogeneity also appears quite early—i.e. during the elastic phase of the macroscopic loading—through localized plasticity that is evidenced by the emergence of slip lines at the grain surfaces in the material [1].

Modeling the behavior of polycrystals while taking into account the individual orientations of their grains is not straightforward because each grain is actually constrained by the other grains of the polycrystal in which it is embedded. The classical assumptions made regarding the heterogeneity of mechanical quantities in polycrystals are the ones of Sachs [2] and Taylor [1] that lead to lower and upper bounds of the polycrystal's macroscopic behavior, respectively. To summarize, Sachs' model assumes that all grains in the polycrystal see the same state of stress while Taylor's model assumes a homogeneous state of strain. For the interested reader, a more comprehensive discussion of these approaches can be found, for example, in Khan and Huang [3] which additionally details the self-consistent schemes that lead to an intermediate behavior between the two bounds (by satisfying conditions of both kinematic compatibility and equilibrium). Nevertheless, these models, which are classified as "mean-field" models, are meant to predict the macroscopic behavior of polycrystals.

Schemes that aim at describing localization both temporally and spatially at the microscopic scale belong to the class of

Electronic supplementary material The online version of this article (https://doi.org/10.1007/s11340-019-00508-0) contains supplementary material, which is available to authorized users.

✉ L. Bodelot
laurence.bodelot@polytechnique.edu

[1] Laboratoire de Mécanique des Solides (LMS), Ecole Polytechnique, CNRS, IPParis, 91128 Palaiseau, France

"full-field" models [4, 5]. They usually consider physical mechanisms down to the atomistic level of dislocations, and compute mechanical quantities within grains that are actually represented either in 2D or 3D. However, simulations are very often carried-out on non-realistic descriptions of the polycrystal via artificial microstructures generated by Voronoi-based tessellation (e.g. [6–9]), even if they describe experimentally-measured statistics of grain orientations. In fact, works integrating both realistic microstructure morphologies and orientation distributions (e.g. [10–12]) focus on the macroscopic response of the polycrystal. Only recently has such an approach involved several hundred grains [13]. Nevertheless, numerical studies focusing on the local response of exact real microstructures (i.e. assigning grain shape and orientation as measured) tend to be computationally expensive, limiting the considered aggregate to a small number of grains (e.g. [14–18]).

In parallel, early experimental studies dedicated to investigating plastic strain localization at the microstructural scale have also been limited to very few grains [14, 15, 19, 20]. More recent studies have exploited advances in imaging speed and resolution as well as improvements in the handling of large datasets, leading to two different approaches. Some have focused on ultra-high-resolution strain fields highlighting localization at the scale of slip lines over a few grains (e.g. [21–24]). Others have conducted strain field measurements at the grain scale, but on a larger number of grains (e.g. [25–32]). The latter studies report common features regarding the development of the plastic network at the surface of the studied samples: early localization, preferential localization at grain boundaries, appearance of a network with 45° localization bands and, very often, the limitation of Schmid factors in pinpointing the first grains that are expected to experience plasticity. Note here that the lack of correlation between plasticity and Schmid factors has been systematically reported for body-centered cubic (BCC) polycrystals, but these polycrystals are known to exhibit abnormal plasticity, as reminded recently by Cho *et al.* [33]. On the other hand, matches between appearance of plasticity and high Schmid factors have been reported in face-centered cubic (FCC) materials (e.g. [23, 25]) and BCC oligocrystals [31], but these matches are based only on a few occurrences: no quantitative or statistical correlation was established in either case. Nevertheless, all authors conclude that grain neighborhoods significantly influence the way that plasticity develops across the aggregate.

Details on how grain parameters and how interactions between grains lead to specific patterns of localization are hence still not clearly understood. Analysis of a large amount of grains is thus needed to reach statistical significance and identify possible quantitative correlations. Here it is worth mentioning that the experimental studies that have actually focused on establishing correlations between plasticity and microstructural parameters on statistically representative datasets (e.g. [34–37]) have only aimed to correlate increasing macroscopic plastic deformation to the evolution of local misorientations within grains. Concurrent strain measurements at the grain scale were never performed. To our knowledge, the only attempt at relating initial microstructural parameters to plastic localization following a statistical approach has been reported in Carroll *et al.* [31], where statistical correlation analyses were focused on the relationship between strain and stress projection factors in a BCC polycrystal.

In this work, initial orientation data collection and grain-scale strain measurements over thousands of grains (to ensure proper statistical significance) are conducted on an FCC polycrystal. Details about data collection and processing are given in the Experimental Methods Section. With this data in hand, the focus is set to obtain experimental insights into the parameters that govern plastic localization and its subsequent organization into a pattern or network. Hence many common microstructural descriptors—such as Schmid factors, Taylor factors, average intragranular misorientation angles or intergranular misorientation angles— are analyzed statistically in connection with the development of a localization network throughout the microstructure. In addition, the full three-dimensional representation of orientations and misorientations are also considered via the corresponding Rodrigues vectors. They are proven to be more informative regarding the localization process than the scalar descriptors that inherently miss part of the orientation data (see Discussion).

Experimental methods

Material and sample

The material examined in this study was 316 L austenitic stainless steel (see chemical composition in Online Resource 1), a single-phase FCC alloy widely used in marine, medical, civil engineering and energy applications. A dog-bone-shaped sample was cut out of the as-received rolled sheet, heat-treated under air at 1200 °C for 2 h, and subsequently water-quenched. The heat-treated sample was then grinded with silicon carbide papers up to grade P2500 and successively polished in colloidal silica solutions containing 60 nm and 20 nm particles, respectively. In addition to removing the oxide layer induced by the heat treatment, this led to the mirror finish necessary for conducting electron back-scattered diffraction (EBSD). The geometry and dimensions of the sample are reported in Fig. 1.

Pyramidal indents were made on the sample's surface within the central zone of interest, as sketched in Fig. 1. They served as the orientation and position references that appear on both optical and scanning electron microscope (SEM) images for subsequent superimposition of local strain data and orientation data, respectively. The pyramidal indents were

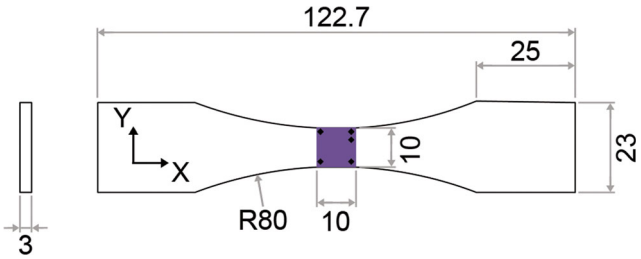

Fig. 1 Sample geometry and dimensions (in mm) showing a sketch of the pyramidal indents made in the zone of interest to serve as orientation and position references. The loading direction is along the horizontal axis of the figure

located a few grains away from the zone of interest so that the plastic deformation they induced did not interfere with the results.

Microstructural characterization

Orientation data was collected within the central zone of the mirror-polished sample by a ZEISS SEM equipped with an EBSD module manufactured by HKL. Orientation collection was performed on a 7.02 mm × 7.02 mm zone that included the indents, with a 15-μm pitch in both the horizontal and vertical directions. Covering such a large area involved using the beam mode (i.e. scanning by deflecting the electron beam) to perform scans smaller than 1 mm by 1 mm, and the stage mode (i.e. displacing the sample by a motorized stage underneath the beam) to repeat single scans and cover the entire area of interest. Indeed, the 1° accuracy of the EBSD module in beam mode is only guaranteed up to a maximum scan area of 1 mm by 1 mm. Data from each single scan was finally stitched together using the Channel 5 EBSD software provided by HKL [38].

Orientation data, given as three Euler angles in the Bunge notation by the Channel 5 software, was then processed by an in-house program [39] to detect grain boundaries from a 5° change in orientation and to subsequently identify grains and their characteristics. Orientation data was also converted to the Rodrigues space in which uniqueness of orientation is ensured [40, 41] (see also Online Resource 1).

Mechanical loading

The 316 L flat dog-bone-shaped sample was submitted to quasi-static uniaxial tension within a 5569 Instron electromechanical load frame equipped with a 50 kN load cell and screw-action grips having serrated faces. The sample was loaded up to a 250 MPa nominal stress in displacement-controlled mode at an equivalent nominal strain rate of 5.10^{-4} s^{-1}, and unloaded in load-controlled mode down to 0 N. The start of the test and the recording by an optical camera installed in front of the sample (see next Section) were triggered simultaneously and were synchronized by using overlapping recording frequencies (100 Hz for load data and 0.2 Hz for optical images). The complete setup is shown in Fig. 2.

In-situ in-plane local strain fields measurements

The sample was imaged during loading by a Jai Pulnix TM-4200 CL CCD camera equipped with 81.5 mm extension tubes and a 50 mm Nikon lens. The camera has a 2048 × 2048 pixels matrix with a 12-bits depth and, in the test configuration, the spatial resolution was 4.2 μm/pixel. Prior to testing, a thin but opaque layer of white acrylic paint was applied to the sample with an airbrush. It was then speckled with black paint, also applied with an airbrush, so as to obtain a random distribution of grayscale patterns. Note that the pyramidal indents were not covered with paint so as to remain visible in the optical images, as seen in the top inset of Fig. 2. Two optical fibers mounted on an infrared-filtered halogen source were symmetrically directed at the sample to obtain uniform lighting. The intensity was adjusted to get a widely distributed range of gray levels in the optical images.

Digital Image Correlation (DIC) was performed using commercial software VIC-2D from Correlated Solutions Inc. The conversion of digital data into continuous data was done through a high-order interpolation scheme (8-tap spline), and the Zero-Normalized Sum of Squared Differences (ZNSSD) correlation criterion was chosen to analyze the images due to its particular insensitivity to noise and light fluctuations [42]. In-plane displacement fields were obtained throughout the loading by using the initial image as the reference; the in-plane strains computed from these displacement fields are finite strains expressed in the reference configuration (Green-Lagrange strain tensor). Finally, the subset size, determined as a compromise between accuracy and resolution, was taken as 17 × 17 pixels with a 3-pixel step size (corresponding to a subset of 71.4 μm × 71.4 μm with a step of 12.6 μm). The lower inset of Fig. 2 provides a zoom onto the speckle as well as a representation of a 17 × 17-pixel subset but note that the full extent of the grayscale gradients, actually spread on 12 bits in the processed data, gets significantly degraded on a standard 8-bit image as the one provided in Fig. 2.

With the large deformations at play, out-of-plane deformation arises at the surface of the sample due to lattice rotation at the microstructural scale. Nevertheless, Sutton *et al.* [43] demonstrated that the error for in-plane strain measurements due to out-of-plane displacement at the surface of the sample is of the order of $\Delta Z/Z$ where ΔZ is the out-of-plane displacement and Z is the distance between the object and the pinhole. In our case, since ΔZ was 22 μm at the last correlation step (ΔZ was measured post-mortem by a Leica DCM8 Confocal microscope) and Z was 63 mm, the maximum error was of the order of 0.035%—acceptable at the largest deformation state. Finally, the systematic error (inherent to the DIC sub-pixel correlation

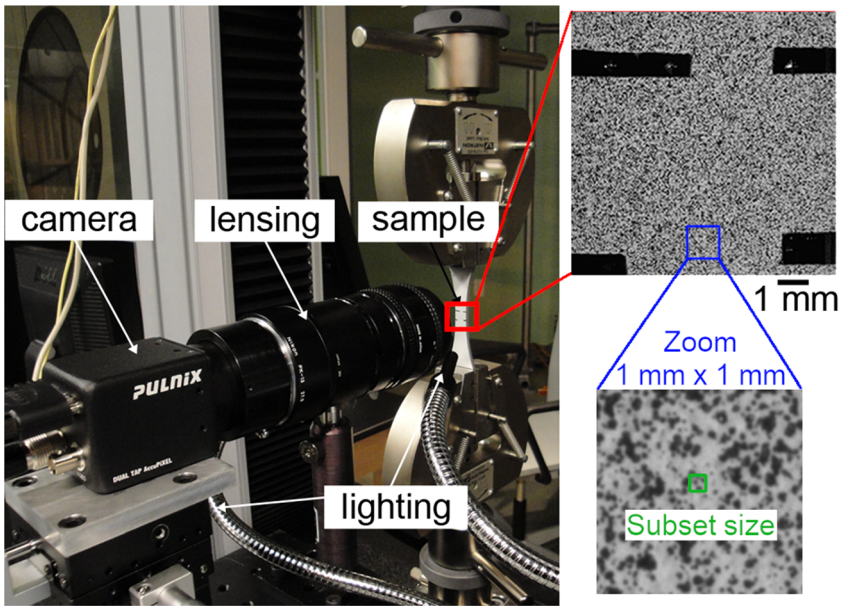

Fig. 2 Experimental setup for in-situ in-plane strain field measurements under uniaxial loading. The inset shows the area of the sample imaged by the camera as well as the speckle pattern

algorithm [44, 45]) and the random error (due to contrast variations during the imaging process [42, 46]) were evaluated for the images at hand and resulted in an uncertainty of 0.012% and 0.076% on the Von Mises strain data, respectively. Note here that the objective was not to obtain a very accurate value of strain but rather to access its relative distribution within the grains of the polycrystal in order to identify the localization network.

Experimental results

Microstructural data

An EBSD orientation map generated by Channel 5 software is presented in Fig. 3a along with the corresponding pole figures in Fig. 3b demonstrating that the material only retained a mild rolling Brass texture after recrystallization.

In the rest of work, all analyses are restricted to a zone of interest (ZOI) that is common to both EBSD and DIC data and is sufficiently far away from the indents, as highlighted by the dashes in Fig. 3a. The grain size distribution was computed from Channel 5 raw data and is reported in Fig. 4a. In this common ZOI containing 2247 grains, the average grain size was 114 μm, thus ensuring that for most of the microstructure (94.3%, see further comment in the first paragraph of the "Statistical analyses and discussion" Section) the subset and step sizes chosen for the DIC computation provided strain data at the microstructural scale. Orientation and misorientation data of the common ZOI are then presented in Fig. 4b and c, respectively. More precisely, in Fig. 4b, the orientation distribution of the common ZOI is plotted in the Rodrigues space.

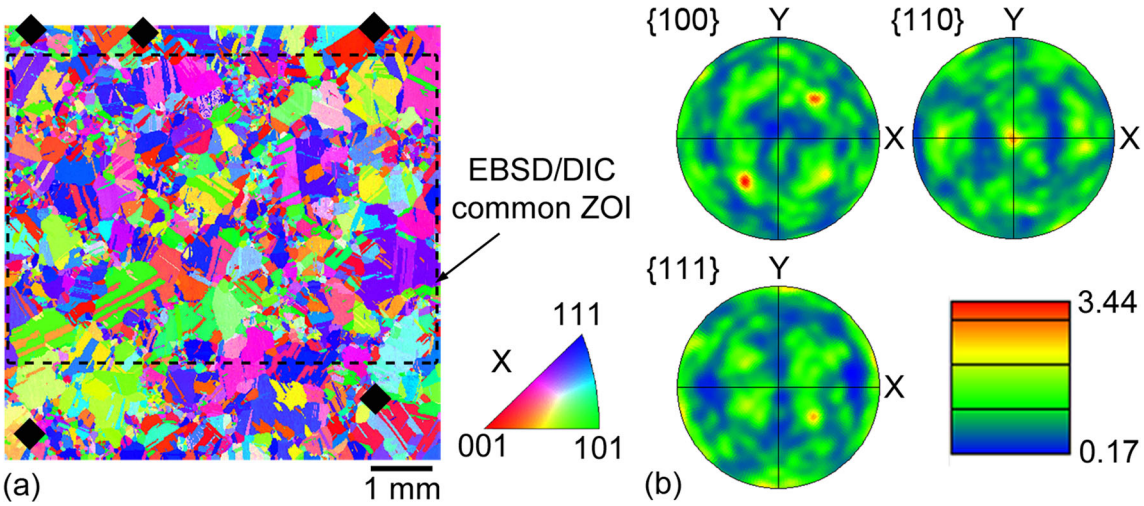

Fig. 3 (a) ESBD map and the (b) corresponding pole figures obtained in the central zone of the sample before loading

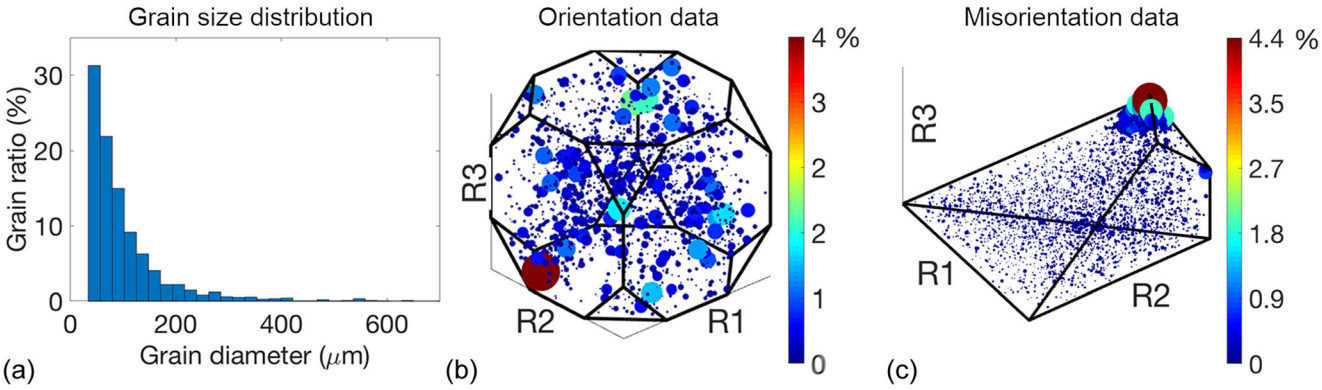

Fig. 4 a) Grain size distribution, b) orientation distribution in the Rodrigues space and c) misorientation distribution in the reduced Rodrigues space. All analyses were performed within the zone of interest common to both the EBSD and DIC data, highlighted by the dashes in Fig. 3a

Each grain average orientation, weighted by its area, was binned in the Rodrigues space and the data in each bin was then normalized to correspond to a statistical intensity within the microstructure (expressed as a percentage). Note that to facilitate the reading of all Rodrigues plots, it was chosen here to make the size of a point/sphere proportional to the intensity/color it represents. A few locations with higher intensity emerged in this orientation distribution as expected from the slight texture seen in Fig. 3b. Fig. 4c then displays the misorientation distribution of the common ZOI. Note here that to ensure uniqueness of misorientation data representation for cubic crystals, one needs to work in a subspace corresponding to 1/48th of the fundamental Rodrigues space (see Online Resource 1 for more details) of Fig. 4b. For each grain, the misorientation with each of its neighbors (weighted by the length of the corresponding boundary) was computed and binned in the Rodrigues subspace. The data in each bin was then normalized to correspond to a statistical intensity within the microstructure, expressed in percent. The misorientation distribution shows fairly uniform distribution throughout the subspace except for a much higher intensity at the highest apex of the subspace that corresponds to Σ3 coincident site lattices (CSL), i.e. twins.

Additionally, average orientation data within each grain was used to compute Schmid and Taylor factors for the statistical analyses reported in the next Section. The corresponding figures are reported in Online Resource 1, and one simply notes here that no specific pattern emerges from either distribution field of Schmid or Taylor factors.

Macroscopic stress-strain curve

The macroscopic nominal stress-strain curve of the tensile test is plotted in Fig. 5, with nominal stress obtained from the force measured by the load cell divided by the initial section of the sample at rest and with strain corresponding to the average value of the Von Mises strains computed by DIC in the zone of interest. Squares are overlaid on this curve to mark the instances at which quantities are reported in the rest of the paper. For reference, the values of strain and stress at each of these instances are listed in Table 1.

Local in-plane strain fields

Three of the pyramidal indents made at the surface of the sample were used to establish the affine plane transformation from the coordinate system of the optical images to that of the coordinate system of the EBSD data extended onto a triple grid. This permitted a projection of the measured strain fields (obtained by DIC computations made on the optical images) onto the initial map of grains (obtained by EBSD) in order to observe the development of the plastic network throughout the microstructure during loading (see Fig. 6). Since data is projected onto a triple grid of the EBSD data, every pixel adjacent to an interface between two grains (detected as a change in orientation) can be colored in black without

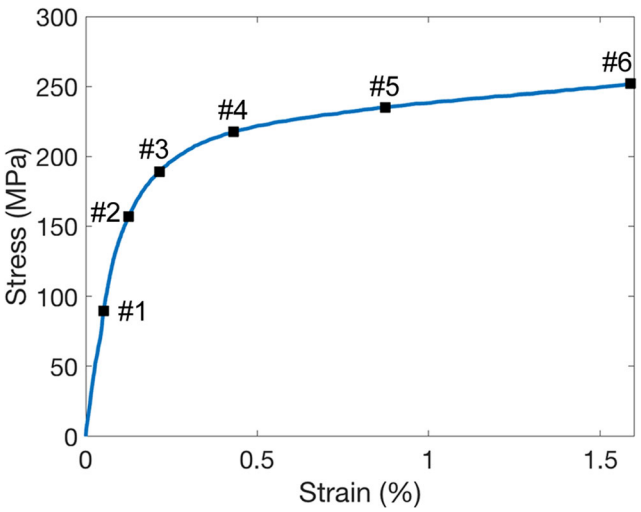

Fig. 5 Macroscopic nominal stress-strain curve. The squares overlaid on the curve mark the instances at which quantities are reported in the rest of the paper

Table 1 Stress and strain values at the instances #1, #2, #3, #4, #5 and #6 marked in Fig. 5

	Instance #1	Instance #2	Instance #3	Instance #4	Instance #5	Instance #6
Strain (%)	0.05	0.13	0.22	0.43	0.87	1.59
Stress (MPa)	89.7	156.8	189.1	217.6	235.1	251.9

covering the whole interior of a grain, hence creating a map of grain boundaries that can be overlaid on top of the aforementioned projected fields. As loading progresses, high values of strains appear closer to grain boundaries throughout the microstructure before spreading into a more and more intense network that takes the form of inclined bands spanning several grains.

Statistical analyses and discussion

Before presenting the conducted statistical analyses, it is important to discuss further the resolutions of the data at hand. EBSD data is based on a 15 μm step size and strain data is obtained with a similar step of 12.4 μm. Hence there is at least one strain data point per orientation data point and several strain data points per grain. However, strain is computed—and thus averaged—over 71.4 μm-side subsets. On the one hand, when one considers the overall spatial distribution of strains, the subset size can be seen as a filter that smoothens out the actual strain gradients in the microstructure but does not change the general distributions/patterns. On the other hand, when one considers the strain data in a small grain, the strain value is affected by the strain in the neighboring grains. Most of the statistical analyses conducted in the paper do not make use of quantitative intragranular data but instead of the general distribution of strains throughout the microstructure by only considering the high strain network (see below). Only the last analysis, that considers strain values within grains, may be affected by the averaging effect of the subset in small grains. Hence, to remove any possible bias on the statistical outcomes, grains with a diameter below 72 μm (5.7% of the considered ZOI) are excluded from all statistical analyses.

As can be seen in Fig. 6, the higher strain values tend to first appear at discrete locations throughout the microstructure before spreading and even connecting as the load increases—hence forming a "network". In each image, a threshold separating higher strain values from lower ones can be defined in order to binarize the strain data and thereby highlight a "high-strain network" or "localization network", as pictured in Fig. 7a (corresponding to instance #4). Here, the strain threshold in each image is taken as the sum of the average Von Mises strain (computed by DIC) and the standard deviation within

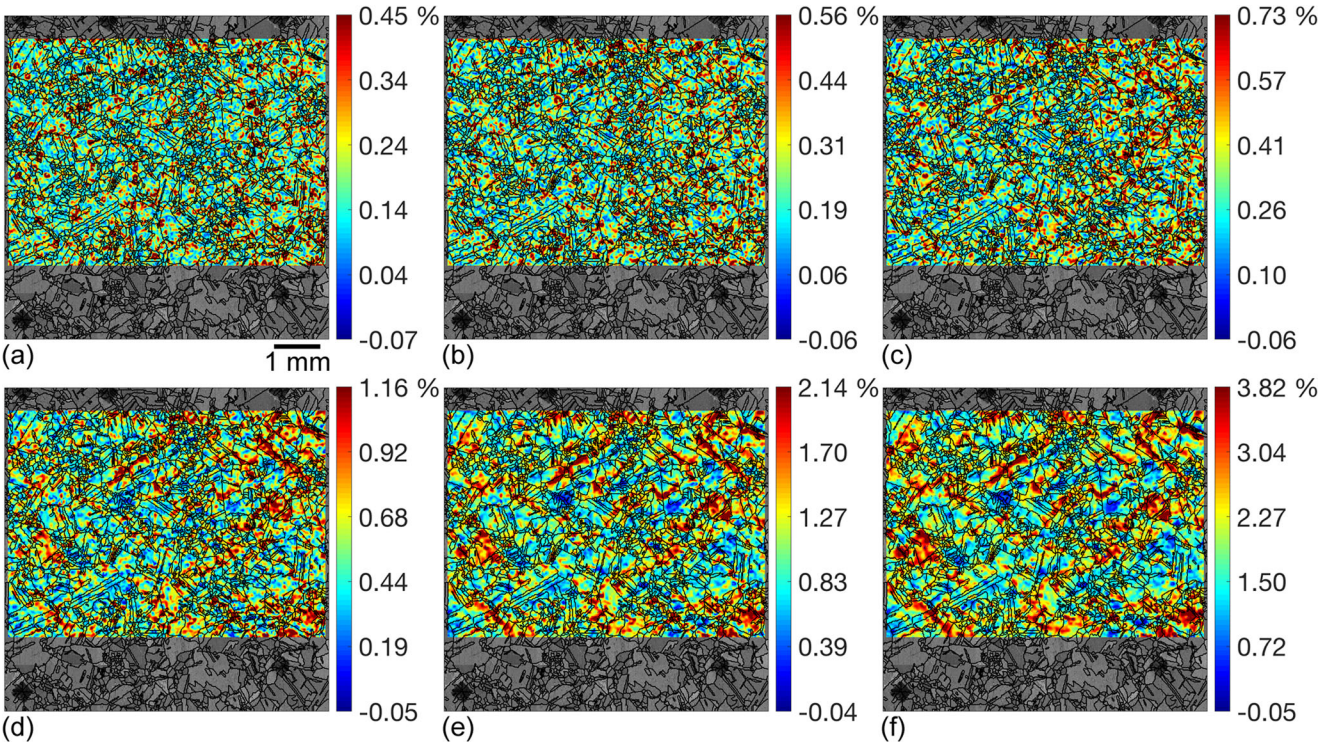

Fig. 6 Von Mises in-plane strain fields at the instances a) #1, b) #2, c) #3, d) #4, e) #5 and f) #6 (marked in Fig. 5) projected onto a map of the initial microstructure of the sample with overlaid grain boundaries

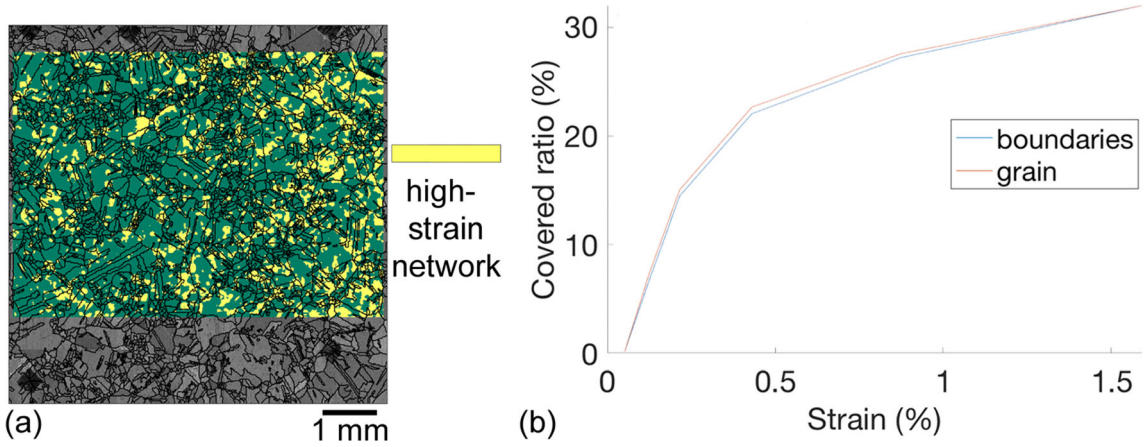

Fig. 7 a) High-strain network at instance #4 projected onto a map of the initial microstructure of the sample with overlaid grain boundaries; zones of high strain are colored in yellow while the rest appears in green. b) Fraction of boundaries and grain area covered by the considered plastic network throughout the tensile loading

the field weighted by the inverse of the relative position of the image during the whole sequence. This weighting allows one to account for the fact that the relative error on strain incurred by the DIC computation is high when strains are low and decreases when strain increases. Since strain fields at each loading step are projected onto the initial microstructure, one can now go beyond the observations of Fig. 6 and analyze quantitatively 1) the relationship between the high-strain network and grain-related data; 2) the relationship between the high-strain network and boundary-related data; and 3) the correlations between strain values and grain-related data. Each analysis is detailed in the next subsections.

Relationship between the high-strain network and grain-related data

In what follows, note that strains are not measured at each boundary (which would require ultra-high-resolution measurements and specific techniques [47]). Instead, the binarized data of the high-strain network (see Fig. 7a) is projected onto the EBSD data in which grain boundaries have been detected (see previous section): this simply makes it possible to determine whether the identified high values of strains fall onto a grain boundary or within a grain. Such information is plotted in Fig. 7b, where it can be seen that the proportion of grain boundaries and grain area covered by the high-strain network remain very close throughout the loading. Considering that the total area of grains is much larger than the total area of boundaries within a microstructure, this result indicates that the high-strain network tends to concentrate primarily at the vicinity of grain boundaries.

Since it is commonly assumed that grains becoming plastic are those with the highest Schmid factor, the distributions of Schmid factors for both the whole ZOI (blue) and the high-strain network (red) are plotted in Fig. 8. Note that the overlapping area between the red and blue histogram bars appears in dark red. At the beginning of loading, the two distributions are very similar (maximum difference of 1.27% at instance #2 for the bin of highest Schmid factors); however, as the loading progresses, the proportion of grains with high Schmid factor becomes larger (4.55% at instance #4 and 5.53% at instance #6) in the distribution of the grains belonging to the high-strain network than in that of the distribution in the whole ZOI. This confirms that grains experiencing plastic localization tend to have a higher Schmid factor (but this is not systematic since less than 20% of grains experiencing high strains have a Schmid factor of 0.5 and grains of much lower Schmid factor also experience high strains). Additionally, it is surprising that the observed tendency is lower at the beginning of the loading than when plasticity is more widespread.

Note that similar assessments of distributions of other grain-related data—such as Taylor factors, kernel average misorientations and average intergranular misorientations (with neighbors of rank 1, 2 and 3)—were done throughout the loading, although none were conclusive.

However, all the previously analyzed quantities are scalar descriptors of orientation data that is by nature a three-dimensional quantity. Hence some data is lost in such descriptors, which is why the three-dimensional orientations of the grains covered by the high-strain network expressed as Rodrigues vectors are now considered. The average orientation of each grain of the ZOI is weighted by the relative area that is covered by the high-strain network at a given loading step. This data can then be binned in the Rodrigues space to represent the proportion of a given orientation, in percentage, belonging to the high-strain network throughout the loading (see Fig. 9). When comparing the orientation distribution of the whole ZOI (Fig. 4b) to the proportions of ZOI orientations belonging to the high-strain network, one notices significant differences in the distributions. Neither at the beginning of the loading nor at the end does the proportion of ZOI orientations belonging to the high-strain network resemble the (area-weighted) orientation

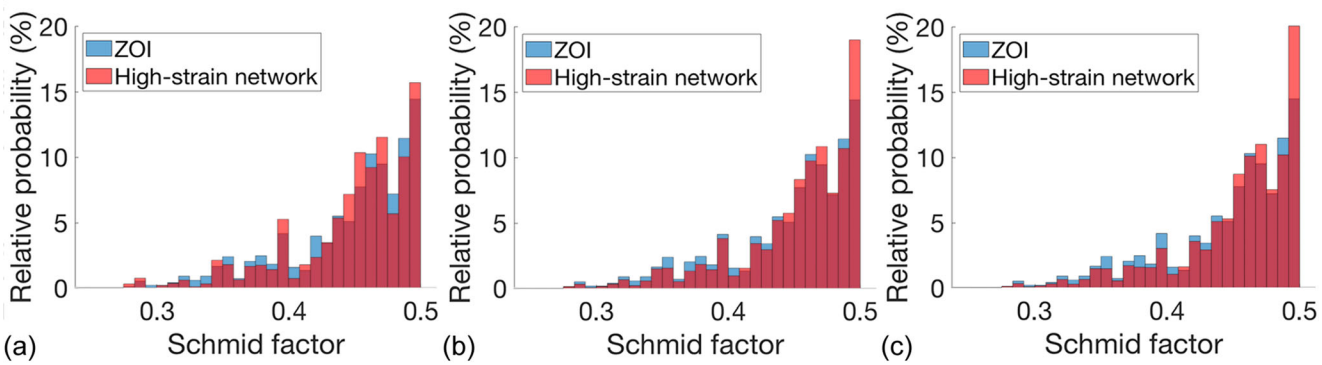

Fig. 8 Distributions of Schmid factors in the whole ZOI (blue) and in the grains belonging to the high-strain network (red) at instances a) #2, b) #4 and c) #6. Note that the overlapping area between the red and blue histogram bars appears in dark red

distribution of the ZOI. This clearly confirms, as is already known [1, 2, 48, 49], that grains experiencing high levels of strain and plasticity are not of random orientation (if that was the case, each distribution in Fig. 9 would look like the orientation distribution of the whole ZOI microstructure). However, no specific pattern (cluster or line) indicating that a certain texture is more prone to plastic localization seems to emerge from the distributions of Fig. 9, including when one plots the distribution as slices of Fig. 9c (see Online Resource 1). It is important to recall though, that the initial microstructure did not exhibit any strong texture either.

Relationship between the high-strain network and boundary-related data

Since the high-strain network has a propensity to concentrate around grain boundaries, focus is set in what follows on gradients of properties across boundaries. In particular, the distributions of Schmid factor ratios across boundaries both in the whole ZOI (blue) and in the high-strain network (red) are plotted in Fig. 10. It can be seen that the proportion of boundaries exhibiting a ratio close to one (i.e., boundaries across which the Schmid factors are nearly identical) is systematically higher in the high-strain network compared to the rest of the microstructure (3.69%, 4.9% and 3.94% at instances #2, #4 and #6, respectively). Here again, the same study can be performed with the corresponding Taylor factor distributions though no significant difference is found between either distribution throughout the loading. Note that these studies can also be carried out by considering the difference of either Schmid or Taylor factors instead of their ratios. In fact, they lead to the same results for the Schmid factors insofar that ratios close to one correspond to gradients close to zero as well as for the Taylor factors, with no significant difference between the distributions. This result indicates that slip transmission tends to be favored at boundaries where Schmid factors are identical; again, this is not systematic since it only applies to at most 23% of the corresponding boundaries.

The distribution of misorientation angles at the boundaries of grains belonging to the high-strain network were also compared to the distribution of misorientation angles at the boundaries of the grains of the whole ZOI, at each step of the loading. There was no predominance of any specific angle among the high-strain network at any point in the loading, but again only a scalar quantity was used to describe a three-dimensional information.

The full three-dimensional misorientation data at boundaries is now considered and is expressed as Rodrigues vectors, weighted by the proportion covered by the high-strain network at a given loading step. This data is binned in the reduced Rodrigues space to represent the proportion of a given misorientation, in percentage, belonging to the high-strain

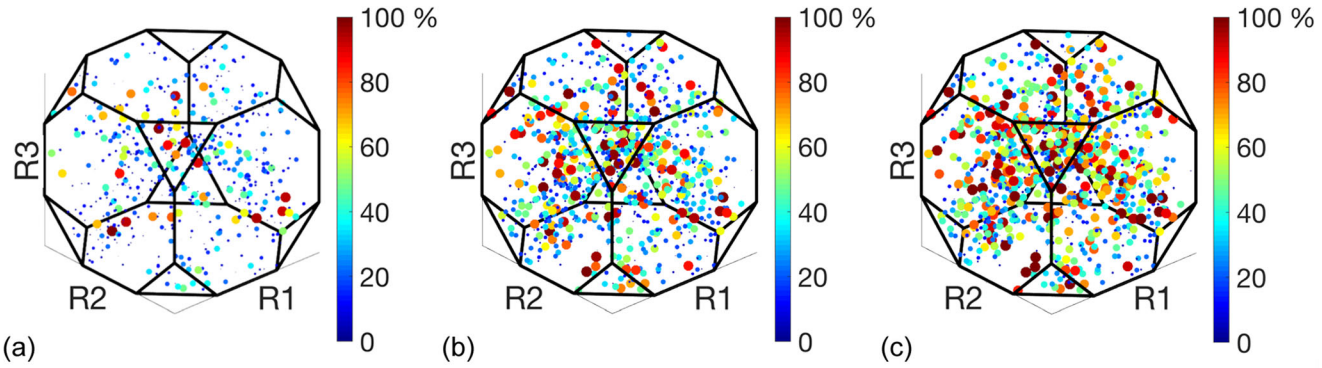

Fig. 9 Proportions of ZOI orientations belonging to the high-strain network at instances a) #2, b) #4 and c) #6

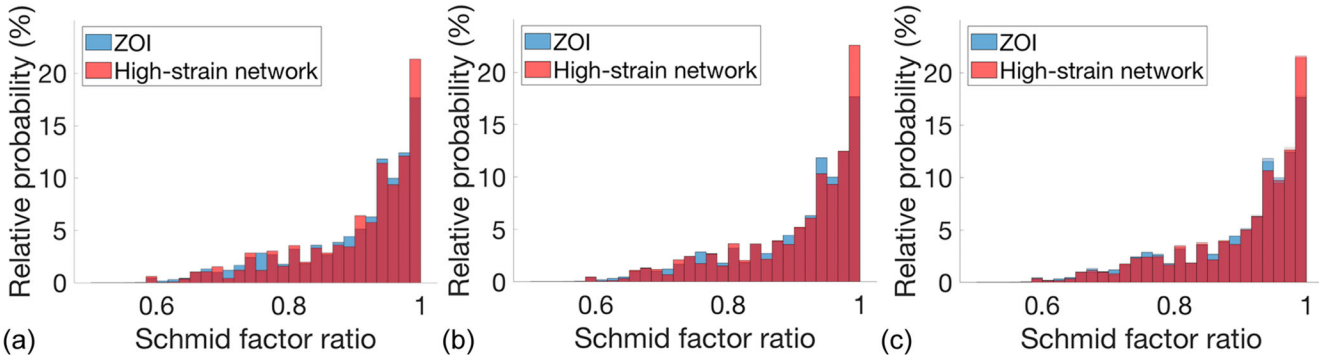

Fig. 10 Distributions of Schmid factor ratios across boundaries in the whole ZOI (blue) and in the grains belonging to the high-strain network (red) at instances a) #2, b) #4 and c) #6. Note that the overlapping area between the red and blue histogram bars appears in dark red

network throughout the loading (see Fig. 11**)**. When comparing the misorientation distribution of the whole ZOI (Fig. 4c) to the proportions of ZOI misorientations that belong to the high-strain network (Fig. 11), one notices significant differences in the distributions. Boundaries that get covered by the high-strain network exhibit misorientations that tend to populate the interior of the Rodrigues subspace even though no specific pattern seems to form (see also the distribution of Fig. 11c represented as slices in Online Resource 1). However, of greater interest are not the boundaries that experience localization but those that resist localization. As a matter of fact, the particular feature that stands out in Fig. 11 is the very low proportion of misorientations close to the highest apex of the subspace (Σ3 CSL) that belong to the high-strain network—even though they are highly represented in the studied microstructure (see Fig.4c). This implies that such misorientations may also play a role in the spread of the plastic network, albeit by opposing localization at boundaries of particular misorientations.

Correlations between strain values and grain-related data

Finally, with the data at hand, it is possible to probe potential statistical correlations arising between the average strain value within a grain (and its standard deviation) and grain-related parameters such as grain size, number of neighbors, mean intragranular misorientation angle, Schmid and Taylor factors, and average intergranular misorientation angle of ranks 1–4. At each loading step, the Spearman rank correlation coefficient [50] can be computed between the strain values and the grain-related data, along with the associated p value that tests the hypothesis of no correlation (beyond a certain threshold) against the hypothesis of a nonzero correlation (below this threshold). Among all tested parameters, the correlations that stand out are between the strain standard deviation and the grain area (see Fig. 12a to c, for which the Spearman rank correlation coefficients are 0.357, 0.420 and 0.423, respectively, and for which all p values are zero). A correlation is also found between the strain values and the Schmid factor since the p value is 0 (see Fig. 12d to f) but, to a much lesser extent, because the Spearman rank correlation coefficients are only 0.149, 0.156 and 0.150, respectively. The positive values of the Spearman rank correlation coefficients in Fig. 12a to c suggest that strain deviation and thus heterogeneities increase with grain size. The low values of the Spearman rank correlation coefficients in Fig. 12d to f demonstrate the very weak correlation between high Schmid factors and high strain values.

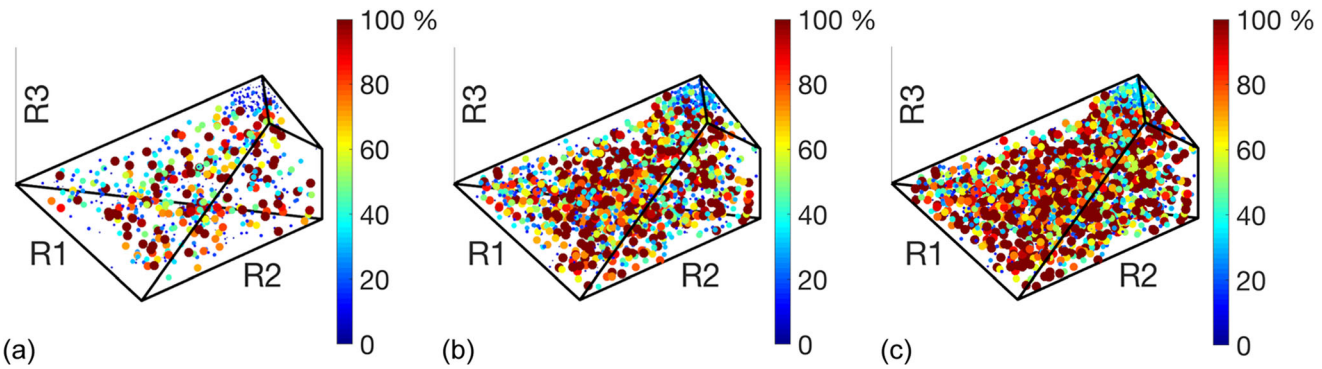

Fig. 11 Proportions of misorientations at boundaries of the ZOI belonging to the high-strain network at instances a) #2, b) #4 and c) #6

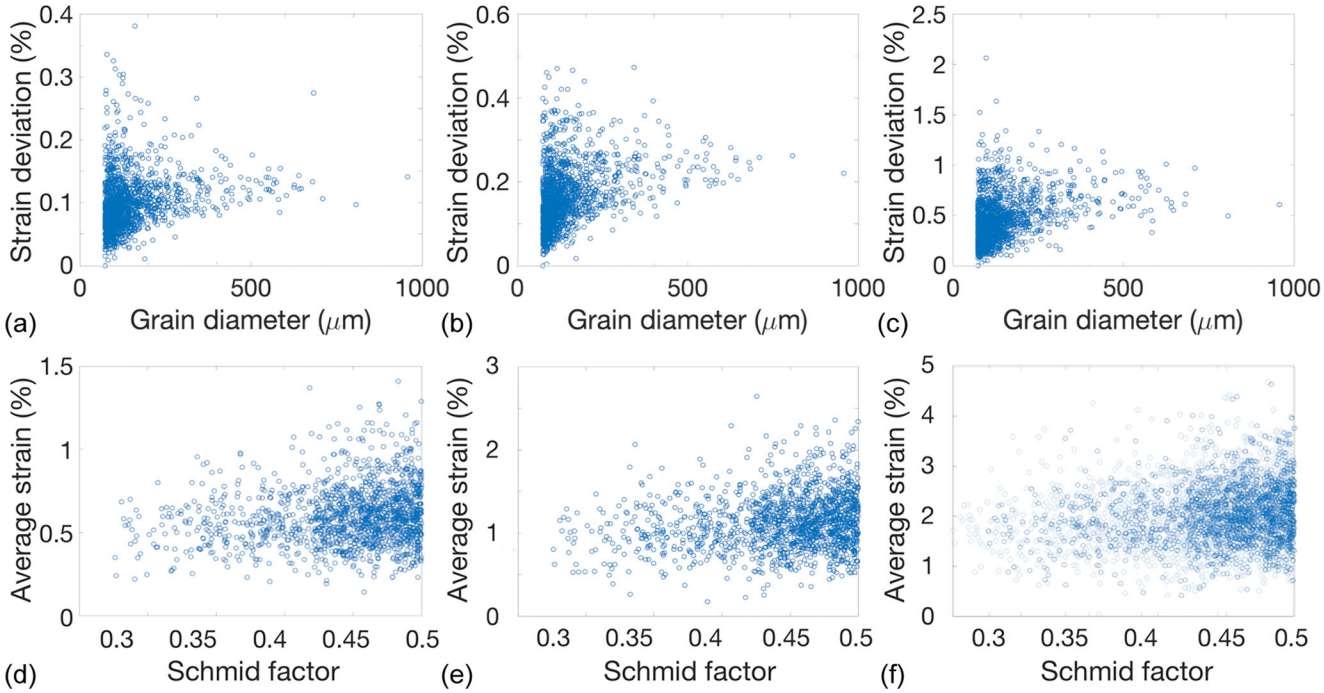

Fig. 12 Relationship between strain standard deviation and grain area at instances a) #2, b) #4 and c) #6. Relationship between average strain within a grain and its Schmid factor at instances d) #4, e) #5 and f) #6

Discussion

Projections of strain fields onto EBSD data has allowed us to study quantitatively and statistically the relationships between the strain localization pattern and initial microstructural features. It is confirmed quantitatively that localization appears primarily at grain boundaries rather than within grains. Localization is also heterogeneous within a grain, with the heterogeneity tending to be more pronounced in larger grains. Statistically, the grains experiencing higher strains show a marginally higher proportion of 0.5 Schmid factors in their distribution than the whole microstructure. Hence the difference is insufficient to systematically associate plasticity with higher Schmid factors. This is even more evident when plotting the average intragranular strain as a function of the Schmid factors. Even though there are some correlations, they remain quite low, as has been pointed out in numerous studies. This limitation of Schmid factors in pinpointing the first grains that are expected to experience plasticity has long been attributed to the influence of grain neighbors. However, even when focusing on quantities that can inform one about the relationships between grains and their neighbors (such as the classical angle of misorientation), no correlation stands out. It was only found that boundaries covered by the high-strain network tend to show a unity ratio of the Schmid factor (implying that slip transmission is higher at boundaries between grains having close Schmid factors)—but again, this is not a systematic relationship.

In fact, the main effect of grain neighbors is that they inherently render invalid the assumption of strain homogeneity within the aggregate—the very assumption that is used to compute the Schmid factors. To solve this issue, Guery *et al.* [18] have proposed to recompute the Schmid factors throughout the loading via a coupling between experiments and numerical simulations, but have also shown that even if correlations are reinforced, they remain rather poor. Additionally, grain neighbor influence comes into play when considering surface information of a three-dimensional aggregate. Knezevic [13] has indeed demonstrated via numerical simulations that 3D effects have a non-negligible influence on strain distributions at the surface of an aggregate although mainly at very high levels of strains.

Thus, considering the full three-dimensional aggregate might not be sufficient. Indeed, if it has long been acknowledged that grain orientations and grain neighborhoods (hence misorientations) both influence localization, only scalar quantities representing three-dimensional orientation and misorientation data have been considered so far in literature, to our knowledge. Even though it remains complicated to compute correlations between a spatial distribution of scalar strain values and three-dimensional information, the plots of Fig. 9 and Fig. 11 show readily that three-dimensional data is worth considering since orientations that exhibit high strains can be highlighted very early in the loading. Similarly, when misorientation angle data does not yield any correlations, analysis of the full three-dimensional misorientation information clearly show that some orientations oppose localization and possibly slip transmission.

Conclusion

Microstructural and strain field data were analyzed over thousands of grains in a 316 L sample under tension to explore the relationships between initial microstructural parameters, localization, and the development of a high-strain network throughout the grains. It is evidenced that localization primarily concentrates at grain boundaries. The limitation of Schmid factors in pinpointing the first grains that should experience plasticity is also confirmed, a shortcoming that is often attributed to the influence of grain neighbors. Of course, the full three-dimensional experimental approach proposed by Pokharel *et al.* [37] could solve the question of the influence of the underlying grain neighbors and give more insight into the physical mechanisms at hand in polycrystalline aggregate deformation processes. However, such experiments and the analysis of their data remain very tedious and costly. Here the proposed protocol is simple to implement and can rapidly provide statistically relevant information. Additionally, it is demonstrated that analyzing three-dimensional orientation and misorientation data to investigate strain localization in polycrystals is a route worth pursuing, even on surface data. It could be indeed valuable to use this approach and collect more data on microstructures with different textures or grain sizes and also to consider other parameters that may affect localization (such as previous heat treatments [51] or surface roughness of the tested sample [52]). Other materials systems, such as BCC, could also be analyzed to investigate whether plastic localization exhibit the same features than observed in this study. With such a breadth of data easily collected, one can also envision employing machine-learning algorithms to detect correlations that may be otherwise difficult to notice when handling three-dimensional data; the final objective being to predict the plastic localization that leads to crack initiation and potential failure from an initial EBSD scan of the surface of the sample.

Acknowledgements Most of the work presented in this paper was conducted at the Graduate Aerospace Laboratory at the California Institute of Technology (GALCIT, Pasadena, California) and supported by the Department of Energy National Nuclear Security Administration under Award Number DE-FC52-08NA28613, which is gratefully acknowledged. The author also thanks Professor Sergio Pellegrino at GALCIT for granting access to the Instron machine in his lab, as well as Professors Guruswami Ravichandran and Michael Ortiz for fruitful discussions.

References

1. Taylor GI (1938) Plastic strains in metals. J Inst Met 62:307–324
2. Sachs G (1929) Zur Ableitung einer Fliessbedingung. Mitteilungen der deutschen Materialprüfungsanstalten. Springer, Berlin, Heidelberg https://doi.org/10.1007/978-3-642-92045-5_12
3. Khan AS, Huang S (1995) Continuum theory of plasticity. John Wiley & Sons, New York
4. Asaro RJ (1983) Crystal Plasticity. J Appl Mech 50:921–934. https://doi.org/10.1115/1.3167205
5. Cuitiño AM, Ortiz M (1992) Computational modelling of single crystals. Modelling Simul Mater Sci Eng 1:225–263. https://doi.org/10.1088/0965-0393/1/3/001
6. Barbe F, Descker L, Jeulin D, and Cailletaud G (2001) Intergranular and intragranular behavior of polycrystalline aggregates. Part 1: F.E. model. Int J Plasticity 17:513–536. https://doi.org/10.1016/S0749-6419(00)00061-9
7. Lebensohn RA, Brenner R, Castelnau O, Rollett AD (2008) Orientation image-based micromechanical modelling of subgrain texture evolution in polycrystalline copper. Acta Mater 56:3914–3926. https://doi.org/10.1016/j.actamat.2008.04.016
8. Patra A, McDowell DL (2016) Crystal plasticity investigation of the microstructural factors influencing dislocation channeling in a model irradiated bcc material. Acta Mater 110:364–376. https://doi.org/10.1016/j.actamat.2016.03.041
9. Abdolvand H, Wright JP, Wilkinson AJ (2018) On the state of deformation in a polycrystalline material in three-dimension: elastic strains, lattice rotations, and deformation mechanisms. Int J Plasticity 106:145–163. https://doi.org/10.1016/j.ijplas.2018.03.006
10. Groeber M, Ghosh S, Uchic MD, Dimiduk DM (2008) A framework for automated analysis and simulation of 3D polycrystalline microstructures. Part 1: Statistical characterization. Acta Mater 56:1257–1273. https://doi.org/10.1016/j.actamat.2007.11.041
11. Groeber M, Ghosh S, Uchic MD, Dimiduk DM (2008) A framework for automated analysis and simulation of 3D polycrystalline microstructures. Part 2: Synthetic structure generation. Acta Mater 56:1274–1287. https://doi.org/10.1016/j.actamat.2007.11.040
12. Qidwai SM, Turner DM, Niezgoda SR, Lewis AC, Geltmacher AB, Rowenhorst DJ, Kalidindi SR (2012) Estimating the response of polycrystalline materials using sets of weighted statistical volume elements. Acta Mater 60:5284–5299. https://doi.org/10.1016/j.actamat.2012.06.026
13. Knezevic M, Drach B, Ardeljan M, Beyerlein IJ (2014) Three dimensional predictions of grain scale plasticity and grain boundaries using crystal plasticity finite element models. Comput Method Appl M 277:239–259. https://doi.org/10.1016/j.cma.2014.05.003
14. Delaire F, Raphanel JL, Rey C (2000) Plastic heterogeneities of a copper multicrystal deformed in uniaxial tension: experimental study and finite element simulations. Acta Mater 48:1075–1087. https://doi.org/10.1016/S1359-6454(99)00408-5
15. Sachtleber M, Zhao Z, Raabe D (2002) Experimental investigation of plastic grain interaction. Mat Sci Eng A-Struct 336:81–87. https://doi.org/10.1016/S0921-5093(01)01974-8
16. Héripré E, Dexet M, Crépin J, Gélébart L, Roos A, Bornert M, Caldemaison D (2007) Coupling between experimental measurements and polycrystal finite element calculations for micromechanical study of metallic materials. Int J Plasticity 23:1512–1539. https://doi.org/10.1016/j.ijplas.2007.01.009
17. Lewis AC, Jordan KA, Geltmacher AB (2008) Determination of Critical Microstructural Features in an Austenitic Stainless Steel Using Image-Based Finite Element Modeling. Metall Mater Trans A 39:1109–1117. https://doi.org/10.1007/s11661-008-9491-8
18. Guery A, Hild F, Latourte F, Roux S (2016) Slip activities in polycrystals determined by coupling DIC measurements with crystal plasticity calculations. Int J Plasticity 81:249–266. https://doi.org/10.1016/j.ijplas.2016.01.008
19. Zhang N, Tong W (2004) An experimental study on grain deformation and interactions in an Al-0.5%Mg multicrystal. Int J Plasticity 20:523–542. https://doi.org/10.1016/S0749-6419(03)00100-1

20. Zhao Z, Ramesh M, Raabe D, Cuitiño AM, Radovitzky R (2008) Investigation of three-dimensional aspects of grain-scale plastic surface deformation of an aluminum oligocrystal. Int J Plasticity 24: 2278–2297. https://doi.org/10.1016/j.ijplas.2008.01.002
21. Di Gioacchino F, Quinta da Fonseca J (2013) Plastic Strain Mapping with Sub-micron Resolution Using Digital Image Correlation. Exp Mech 53:743–754. https://doi.org/10.1007/s11340-012-9685-2
22. Patriarca L, Abuzaid W, Sehitoglu H, Maier HJ (2013) Slip transmission in bcc FeCr polycrystal. Mater Sci Eng A-Struct 588:308–317. https://doi.org/10.1016/j.msea.2013.08.050
23. Kammers AD, Daly S (2013) Digital Image Correlation under Scanning Electron Microscopy: Methodology and Validation. Exp Mech 53:1743–1761. https://doi.org/10.1007/s11340-013-9782-x
24. Zhang Z, Lunt D, Abdolvand H, Wilkinson AJ, Preuss M, Dunne FPE (2018) Quantitative investigation of micro slip and localization in polycrystalline materials under uniaxial tension. Int J Plast 108: 88–106. https://doi.org/10.1016/j.ijplas.2018.04.014
25. Tschopp MA, Bartha BB, Porter WJ, Murray PT, Fairchild SB (2009) Microstructure-Dependent Local Strain Behavior in Polycrystals through In-Situ Scanning Electron Microscope Tensile Experiments. Metall Mater Trans A 40:2363–2368. https://doi.org/10.1007/s11340-013-9782-x
26. Efstathiou C, Boyce DE, Park JS, Lienert U, Dawson PR, Miller MP (2010) A method for measuring single-crystal elastic moduli using high-energy X-ray diffraction and a crystal-based finite element model. Acta Mater 58:5806–5819. https://doi.org/10.1016/j.actamat.2010.06.056
27. Abuzaid WZ, Sangid MD, Carroll JD, Sehitoglu H, Lambros J (2012) Slip transfer and plastic strain accumulation across grain boundaries in Hastelloy X. J Mech Phys Solids 60:1201–1220. https://doi.org/10.1016/j.jmps.2012.02.001
28. Littlewood PD, Wilkinson AJ (2012) Local deformation patterns in Ti-6Al-4V under tensile, fatigue and dwell fatigue loading. Int J Fatigue 43:111–119. https://doi.org/10.1016/j.ijfatigue.2012.03.001
29. Padilla HA, Lambros J, Beaudoin AJ, Robertson IM (2012) Relating inhomogeneous deformation to local texture in zirconium through grain-scale digital image correlation strain mapping experiments. Int J Solids Structures 49:18–31. https://doi.org/10.1016/j.ijsolstr.2011.09.001
30. Walley JL, Wheeler R, Uchic MD, Mills MJ (2012) In-Situ Mechanical Testing for Characterizing Strain Localization During Deformation at Elevated Temperatures. Exp Mech 52:405–416. https://doi.org/10.1007/s11340-011-9499-7
31. Carroll JD, Clark BG, Buchheit TE, Boyce BL, Weinberger CR (2013) An experimental statistical analysis of stress projection factors in BCC tantalum. Mater Sci Eng A-Struct 581:108–118. https://doi.org/10.1016/j.msea.2013.05.085
32. Carroll JD, Abuzaid W, Lambros J, Sehitoglu H (2013) High resolution digital image correlation measurements of strain accumulation in fatigue crack growth. Int J Fatigue 57:140–150. https://doi.org/10.1016/j.ijfatigue.2012.06.010
33. Cho H, Bronkhorst CA, Mourad HM, Mayeur JR, Luscher DJ (2018) Anomalous plasticity of body-centered-cubic crystals with non-Schmid effect. Int J Solids Struct 139-140:138–149. https://doi.org/10.1016/j.ijsolstr.2018.01.029
34. Mishra SK, Pant P, Narasimhan K, Rollett AD, Samajdar I (2009) On the widths of orientation gradient zones adjacent to grain boundaries. Scripta Mater 61:273–276. https://doi.org/10.1016/j.scriptamat.2009.03.062
35. Yoda R, Yokomaku T, Tsuji N (2010) Plastic deformation and creep damage evaluations of type 316 austenitic stainless steels by EBSD. Mater Charact 61:913–922. https://doi.org/10.1016/j.matchar.2010.05.006
36. Allain-Bonasso N, Wagner F, Berbenni S, Field DP (2012) A study of the heterogeneity of plastic deformation in IF steel by EBSD. Mater Sci Eng A-Struct 548:56–63. https://doi.org/10.1016/j.msea.2012.03.068
37. Pokharel R, Lind J, Li SF, Kenesei P, Lebensohn RA, Suter RM, Rollett AD (2015) In-situ observation of bulk 3D grain evolution during plastic deformation in polycrystalline Cu. Int J Plasticity 67: 217–234. https://doi.org/10.1016/j.ijplas.2014.10.013
38. Oxkford Instruments (2007) HKL Channel 5 Manual
39. Bodelot L, Ravichandran G (2014) Experimental determination of a representative texture and insight into the range of significant neighboring grain interactions via orientation and misorientation statistics. Int J Mater Res 105:117–129. https://doi.org/10.3139/146.111007
40. Becker R, Panchanadeeswaran S (1989) Crystal Rotations Represented as Rodrigues Vectors. Texture Microstruct 10:167–194. https://doi.org/10.1155/TSM.10.167
41. Morawiec A, Field DP (1996) Rodrigues Parameterization for Orientation and Misorientation Distributions. Philos Mag A 73: 1113–1130. https://doi.org/10.1080/01418619608243708
42. Sutton MA, Orteu J, Schreier HW (2009) Image Correlation for Shape, Motion and Deformation Measurements. Basic Concepts, Theory and Applications. Springer, New York
43. Sutton MA, Yan JH, Tiwari V, Schreier HW, Orteu JJ (2008) The effect of out-of-plane motion on 2D and 3D digital image correlation measurements. Opt Laser Eng 46:746–757. https://doi.org/10.1016/j.optlaseng.2008.05.005
44. Schreier HW, Braasch JR, Sutton MA (2000) Systematic errors in digital image correlation caused by intensity interpolation. Opt Eng 39:2915–2921. https://doi.org/10.1117/1.1314593
45. Hild F, Roux S (2006) Digital Image Correlation: from Displacement Measurement to Identification of Elastic Properties - a Review. Strain 42:69–80. https://doi.org/10.1111/j.1475-1305.2006.00258.x
46. Bornert M, Brémand F, Doumalin P, Dupré J, Fazzini M, Grédiac M, Hild F, Mistou S, Molimard J, Orteu J, Robert L, Surrel Y, Vacher P, Wattrisse B (2009) Assessment of Digital Image Correlation Measurement Errors: Methodology and Results. Exp Mech 49:353–370. https://doi.org/10.1007/s11340-008-9204-7
47. Doquet V, Barkia B (2016) Combined AFM, SEM and crystal plasticity analysis of grain boundary sliding in titanium at room temperature. Mech Mater 103:18–27. https://doi.org/10.1016/j.mechmat.2016.09.001
48. Schmid E, Boas W (1950) Plasticity of Crystals with Special Reference to Metals. F. A. Hughes, London
49. Bishop JFW (1953) A theoretical examination of the plastic deformation of crystals by glide. Philos Mag 44:51–64. https://doi.org/10.1080/14786440108520274
50. Spearman C (1904) The Proof and Measurement of Association between Two Things. Am J Psychol 15:72–101
51. Kurzydlowski KJ, Czerepko W (1994) On the localization of the plastic flow in polycrystals of austenitic stainless steel. Key Eng Mat 97(98):501–505. https://doi.org/10.4028/www.scientific.net/KEM.97-98.501
52. Guilhem Y, Basseville S, Curtit F, Stéphan J, Cailletaud G (2018) Numerical analysis of the effect of surface roughness on mechanical fields in polycrystalline aggregates. Modelling Simul Mater Sci Eng 26:045004. https://doi.org/10.1088/1361-651X/aab217